Comparison of thermo-hydraulic performance among different 3D printed periodic open cellular structures

DOI:
[10.1016/j.cej.2024.152005](10.1016/j.cej.2024.152005)

Document status and date:
Published: 15/07/2024

Document Version:
Publisher's PDF, also known as Version of Record (includes final page, issue and volume numbers)

Please check the document version of this publication:

• A submitted manuscript is the version of the article upon submission and before peer-review. There can be important differences between the submitted version and the official published version of record. People interested in the research are advised to contact the author for the final version of the publication, or visit the DOI to the publisher's website.
• The final author version and the galley proof are versions of the publication after peer review.
• The final published version features the final layout of the paper including the volume, issue and page numbers.

Link to publication

Comparison of thermo-hydraulic performance among different 3D printed periodic open cellular structures

S. Richard [a,d,*], D. Tasso [a], M. Rajana [a], A Saker [a], A. Ramirez Santos [a], C. Makhloufi [a], N. Meynet [a], B. Hary [b], S. Nardone [b], G. Marino [c], M. Thomas [c], C. Italiano [c], A. Vita [c], F. Gallucci [d]

[a] *ENGIE Lab CRIGEN, 4 Rue Joséphine Baker, Stains, France*
[b] *ENGIE Laborelec, Rodestraat 125, 1630 Linkebeek, Belgium*
[c] *CNR-ITAE, Via Salita S. Lucia sopra Contesse n.5, S. Lucia, 98126 Messina, Italy*
[d] *Sustainable Process Engineering, Chemical Engineering and Chemistry, Eindhoven University of Technology, Den Dolech 2, 5612 AZ, Eindhoven, the Netherlands*

ARTICLE INFO

ABSTRACT

As additive manufacturing of periodic open cellular structures (POCS) is gaining interest in structured catalytic reactor research, this work seeks to thermohydraulically compare the well-known Kelvin lattice structure with the lesser-researched BCC and gyroid lattice structures. Using a combined CFD (Computational Fluid Dynamic) and experimental approach, the selected POCS are fabricated through Laser Powder Bed Fusion (LPBF), characterized, and subsequently subjected to numerical analysis. From the manufacturability point of view, the 3D printed samples closely matched their CAD designs, showing a maximum porosity deviation of 15% below design values. A CFD model, validated through pressure drop experiment, was employed to compare the POCS designs on shared geometric attributes such as specific surface area and porosity. While all structures exhibited comparable performance in term of heat and momentum transfer, our findings suggest that the Gyroid lattice may provide the optimal balance between momentum and heat transfer rates in low-velocity region. Conversely, the BCC configuration may be more favourable at higher velocity. An Ergun-like correlation was also developed and validated for each lattice type, with a Mean Absolute Percentage Error (MAPE) below 10%. Our pressure drop results align quite well with existing literature correlations, showing a MAPE under 20%. Concerning heat transfer, the values forecasted in this research show a reasonable alignment with literature's results, though they tend to be on the lower spectrum.

1. Introduction

In the evolving landscape of chemical engineering, there is a growing need for advanced catalytic technologies that are efficient, safe, and environmentally friendly. The traditional "packed bed reactors" (PBRs), while known for their straightforward design and substantial catalyst loading, face challenges such as flow channelling, inconsistent flow, and constraints in both mass and heat transfer. Additionally, these reactors often experience pronounced pressure drops, which amplify operational expenditures [1]. Designing these reactors requires a grasp of the trade-offs involved: while smaller catalyst pellets can enhance catalyst use and heat transfer, they also increase pressure drops. The complexity of balancing these factors make optimal designs elusive. In response, alternative catalytic supports have been developed, offering improved design flexibility and control over fluid flow, species distribution, and heat transfer. For example, the nature-inspired honeycomb design showcases advantages like a high surface-to-volume ratio, enabling efficient gas-to-solid mass and heat transfer rates, all while ensuring low pressure drops in a homogeneous structure [2 3]. Similarly, Open-cell foams (OCF) [4] have been introduced, characterized by their tortuous solid matrix of interconnected open cells. The diverse solid ligaments within OCFs foster fluid mixing, leading to heightened fluid–solid transfer rates. Recently, there has been a surge in interest surrounding Periodic Open-Cell Structures (POCS) as a novel catalytic support [5]. These supports are defined by their structured network of consistently shaped, interconnected unit cells windows forming a three-dimensional framework. Combining the advantages of OCFs and honeycombs, POCS effectively manage both axial and radial heat transfer while maintaining a uniform structure with a reasonable pressure drop. Using additive manufacturing, also referred to as 3D printing, POCS could offer a new way to design catalytic supports tailored to specific

---

Nomenclature

Acronyms

BCC	Body-Centered Cubic Cell
CAD	Computer-Aided Design
CFD	Computational Fluid Dynamic
DNS	Direct Numerical Simulation
FDM	Fused Deposition Modelling
LPBF	Laser Powder Bed Fusion
MAPE	Mean Absolute Percentage Error
OCF	Open-Cell Foam
POCS	Periodic Open Cell Structure
PBR	Packed bed reactor
RANS	Reynolds-Averaged Navier-Stokes
RMSE	Root Mean Square Error
SLM	Selective Laser Melting
SEM	Scanning Electron Microscopy
TPMS	Triply Periodic Minimal Surface

Latin letters

d_c	Cell length(m)
d_s	Strut diameter or gyroid thickness(m)
h	Surface heat transfer coefficient (W.m^{-2}.K^{-1})
h_v	Volumetric heat transfer coefficient (W.m^{-3}.K^{-1})
L_{char}	Characteristic length (m)
S_{POCS}	Total POCS surface (in contact with fluid)(m^2)
T	Fluid temperature (°C)
T_{ref}	Reference temperature (either the inlet fluid temperature or the volume fluid averaged temperature). (°C)
v	Fluid velocity(m.s^{-1})

Greek letters

μ	Dynamic viscosity (Pa.s)
ϵ	Porosity ($-$)
λ	Fluid thermal conductivity (W.m^{-1}.K^{-1})
ρ	Fluid density (kg.m^{-3})
$\Phi(i)$	Elementary power exchanged through each i cell's surface adjacent to the solid (W)

---

needs [6 7]. A range of 3D printing methods have already been used to produced POCS with precision, including robocasting [8] selective electron beam melting (SEBM) [9], selective laser melting (SLM) [10 11], direct metal laser sintering (DMLS) and stereolithography [12]. The literature also present a variety of unit cell types such as cubic [9 13 14], diamond [12 15 13], octet [16] and triply periodic minimal surface (TPMS) [17 18 19 20]. Commonly, these unit cells combine cylindrical struts and spheres at the junctions, though some studies build POCS by subtracting spheres [21 22]. The Kelvin cell [23 24 22 25 26 27 28], also known as Tetrakaidecahedron or Vine tile, is particularly popular because of its widespread utilization to represent OCF. Some studies have already showed encouraging outcome regarding catalytic POCS tested in reactive environment including application in methanation [17 8] or hydrogen production through ammonia cracking [29] or methanol reforming [21].

To effectively design POCS reactors, understanding transport phenomena is crucial. Previous research has often focused on heat transfer [26 30 31 18 19] and pressure drop [18 31], using Computational Fluid Dynamics (CFD) for analysis. These simulations allow for systematic exploration of different topologies and the derivation of engineering correlations. For instance, Das et al. [32] employed Direct Numerical Simulation (DNS) to study the friction factor of a Kelvin lattice and, based on simulations across several topologies, formulated a correlation. Similarly, Rambabu et al. (2021) [33] employed RANS simulations to derive a pressure drop correlation for the same lattice structure. Some researchers compared these structures with alternative catalyst support [34 28 34 35]. For instance, Lucci et al. (2017) [40] made a comparison between an OCF and a Kelvin cell lattice with similar porosity and surface area. They observed that the Kelvin cell generally had a better mass transfer − pressure drop trade off compared to its foam counterpart. In a similar vein, some researchers also contrasted different unit cells types [26 14 36 37 38]. For example, Kaur et al. (2020) [26] explored the heat-transfer and pressure drop properties of four cell types and noted that the Octet structure outperformed the others in both pressure drop and Nusselt number. While numerous theoretical thermohydraulic studies are available, there is only a handful of experimental works on metallic POCS [9 39 15 40 41 16 30]. For instance, Klump et al. (2014) [9] utilized the selective electron beam melting (SEBM) method to study Ti-based cubic cell geometries. Their research emphasized the distinct flow properties arising from different cell orientations. In contrast, Rebelo et al. (2018) [39] examined the design parameters of cubic cells, finding only minimal impact of angular orientation on pressure drop. They employed direct metal laser sintering

(DMLS) for manufacturing and showcased cubic-cell foams 3D printed in aluminum. In an original approach Do et al. (2020) [40] delved into an interpenetrating POCS structure based on diamond geometry fabricated by fused deposition modeling. They introduced this design as adaptable, capable of adjusting flow characteristics to match process requirements. Chaudhari et al. (2019) [16] inspected the performance of the Octet-truss lattice structure made of AlSiMg alloy. They derived friction factor correlations for this specific sample. Busse et al. (2018) [30], conducted heat transfer experiments on SEBM printed cubic cells (Ti$_6$Al$_4$V, IN718) and formulated new heat transfer correlations. They demonstrated that enhancing the wall coupling between the POCS structure and the tube shell can notably increase the overall heat transfer coefficient. Specifically, a fully coupled structure displayed a heat transfer coefficient 3.5 times greater than a loosely structured counterpart.

Though there is obvious advancement in POCS thermohydraulic research, most studies focus on specific cell types, mainly Kelvin cells. There is a lack of comprehensive comparisons of various POCS designs, with many yet to be studied. Additionally, current literature sometimes presents conflicting findings, and even established POCS configurations have debated correlations. To address this, the present study aims at contrasting the thermohydraulic performance of three lattices: the popular Kelvin cell, and the lesser-studied BCC and gyroid lattice as represented in Fig. 1. To achieve this aim, a holistic approach is employed, combining both CFD and experimental analyses. Within this framework, the selected POCS are printed using LPBF, comprehensively characterized, and then analysed numerically. This approach enables the derivation of Ergun-like correlations for the precise description of pressure drop across the selected samples.

2. Experimental

2.1. POCS structure characteristics

POCS samples were produced using the LPBF (Laser Powder Bed Fusion) technique based on CAD designs, resulting in cylindrical models of 10 mm diameter and 15 mm height. These models represent three cell types: body-centered cubic, Kelvin, and gyroid, each with design variations to obtain different surface areas and porosities. The following feedstock materials were used for the printing: AlSi10Mg, IN625, and CuNi2SiCr. The first two materials were printed at ENGIE Laborelec using a SLM280 LPBF machine while the last material was printed and heat treated by Zare (under the BEAMIT group). AlSi10Mg is notable for its heat-transfer capabilities due to its high thermal conductivity but is
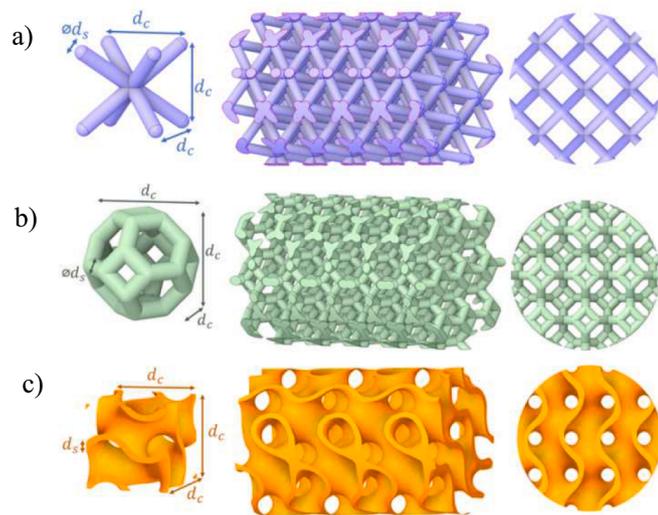
Fig. 1. POCS structure investigated in this work a) BCC (Top, purple) b) Kelvin cell (Middle, green) c) Gyroid (Bottom, orange); d_c represents the cell dimension and d_s indicates the thickness of the strut. (For interpretation of the references to colour in this figure legend, the reader is referred to the web version of this article.)

suitable for processes requiring limited temperature (e.g. such as Fischer-Tropsch synthesis or methanol steam reforming). CuNi2SiCr also has high thermal conductivity and can withstand up to 500 °C, suitable for higher temperature processes (e.g. methane reforming with membrane reactors or ammonia cracking). On the other hand, IN625 material could stand out for Joule heating applications whilst remaining very suitable for high-temperature environments (at least up to 700 °C). Table 1 summarizes the design parameters of the CAD models, including materials, strut diameter, cell length, porosity, and specific surface. The latter two properties are defined as per Eq. (1) & Eq. (2) respectively. A noteworthy observation pertains to the post-processing of the Kelvin 3–0,6 model in Al alloy and its counterpart in Cu alloy which underwent a sand blasting procedure. All other configurations in AlSi10Mg and IN625 were preserved in their as-built state.

$$\epsilon = \frac{Void\,volume}{Total\,volume} = 1 - \frac{Solid\,volume}{Total\,volume} \tag{1}$$

$$S_v = \frac{Total\,POCS\,area}{Total\,volume} \tag{2}$$

2.2. Geometrical characterization & pressure drop measurements

The samples were analysed using a Keyence VHX-7000 digital optical microscope. Detailed images of the POCS were taken with VHX-E20 (low magnification objective lens: 20–100×) and VHX-E100 (medium magnification objective lens: 100–500×) lenses. Measurements were made at various points on the struts and windows to identify any discrepancies from the CAD model. Further in-depth inspection was conducted with pycnometry and Scanning Electron Microscopy (SEM). A Multivolume Pycnometer 1305 (Micromeritics) was used to obtain true volume and relative densities/porosities of POCS (This device ensures a density calculation accuracy of ±0.1 to 0.2 % and a volume measurement accuracy of ±0.2 %). The sample chamber is initially pressurized with helium. The later expansion of this gas into a precisely measured volume induces a drop in pressure. The sample's volume, density and the relative porosity can then be readily calculated based on the two pressure readings. SEM analyses were performed with a Philips XL-30 FEG operated at 5–20 kV. After characterization, the pressure drop of the samples was assessed using two different methods. In method "A", a U-tube manometer (internal diameter = 1 cm, length = 13.5 cm) connected to a reactor containing the sample measured the pressure drop across various superficial velocities. N_2 at ambient temperature was introduced, and its flow rate was measured with a digital flowmeter (Agilent ADM 2000). The water height differential in the U-tube was converted to a pressure drop value using Stevin's law. For method "B", a micromanometer (DeltaOhm HD 2114.2, with an instrumental resolution of 0.005 mbar and an accuracy of ±0.3 %) was used, attached to the reactor housing the POCS. Similarly, N_2 was introduced at room temperature and its rate was determined by a different digital flowmeter different digital flowmeter (MesaLabs Defender 530+, volumetric accuracy: 0.75 %, standardized accuracy: 1 %) with velocities ranging from 0–10 m/s. Table 2 summarizes the measurement techniques utilized throughout the experimental campaign. The pressure ports are located 6 cm from both the inlet and outlet of the sample (external

Table 1

Geometrical features of the CAD design cell parameters printed. The porosity and specific surface area refer to the theoretical ones of the CAD. Structures denoted with a 'sb' superscript have been sandblasted; others are as-built.

Cell type	Material	Cell length [mm]	Strut diameter [mm]	Theoretical Porosity %	Theoretical Specific surface area [cm^{-1}]	Denomination
Kelvin	AlSi10Mg	3	0.6	0.79	12.16	Kelvin 3-0.6-Al[sb]
	CuNi2SiCr	3	0.6	0.79	12.16	Kelvin 3-0.6-Al[sb]
	IN625	3	0.6	0.79	12.16	Kelvin 3-0.6-Ni
	IN625	4	0.6	0.89	6.52	Kelvin 3-0.6-Ni
	IN625	3	0.8	0.66	13.70	Kelvin 3-0.6-Ni
	IN625	3	0.4	0.9	8.89	Kelvin 3-0.6-Ni
	IN625	1.5	0.3	0.77	23.46	Kelvin 3-0.6-Ni
	IN625	4	0.8	0.81	7.78	Kelvin 3-0.6-Ni
	IN625	2	0.4	0.78	17.15	Kelvin 3-0.6-Ni
	IN625	2	0.6	0.55	17.97	Kelvin 3-0.6-Ni
BCC	AlSi10Mg	3	0.6	0.83	10.79	BCC 3-0.6-Al
	IN625	2	0.4	0.83	16.26	BCC 3-0.6-Ni
	IN625	2	0.6	0.64	19.84	BCC 3-0.6-Ni
	IN625	3	0.4	0.92	8.09	BCC 3-0.6-Ni
	IN625	3	0.6	0.83	10.79	BCC 3-0.6-Ni
	IN625	3	0.8	0.71	12.68	BCC 3-0.6-Ni
	IN625	4	0.6	0.912	6.30	BCC 3-0.6-Ni
	IN625	4	0.8	0.852	7.76	BCC 3-0.6-Ni
Gyroid	In625	3	0.2	0.794	20.4	Gyr 5-0.34-Ni
	In625	3	0.3	0.694	20.1	Gyr 5-0.34-Ni
	In625	3	0.4	0.616	19.5	Gyr 5-0.34-Ni
	In625	5	0.34	0.79	12.3	Gyr 5-0.34-Ni

Table 2
Measurement techniques employed during the pressure drop experimental campaign.

Sample	Measurements
BCC 3-0,6 (Al alloy)	1 series (A)
BCC 3-0,6 (Ni alloy)	1 series (B)
Kelvin 3-0,6 (Al alloy)	1 series (A)
Kelvin 3-0,6 (Cu alloy)	1 series (A)
Kelvin 3-0,6 (Ni alloy)	1 series (A)
Kelvin 3-0,8 (Ni alloy)	1 series (A)

diameter = 1 cm, length = 1.5 cm) positioned in the middle of the reactor tube. To mitigate the potential impact of the reactor setup, blank tests (without the structured support) have been caried out for each flow rate and sample used. These blank tests allow to isolate and subtract any interference arising from pressure loss attributable to the reactor setup and the positioning of pressure ports to ensure that the measured pressure drop accurately reflected the characteristics of the samples under investigation, independent of any external influences.

3. Numerical investigation

3.1. CFD modelling

To complement experimental data and gain deeper insights into POCS behavior under specific topologies, RANS (Reynolds-Averaged Navier-Stokes) simulations are deployed within Ansys Fluent (version 2023 R1). The simulations address both momentum and heat transfer aspects in two separate studies. Fig. 2 illustrates the computational domain, mirroring the experimental setup, and highlights the applied boundary conditions. Inlet velocities ranged between 1 and 9 m/s, while the outlet was maintained to atmospheric pressure. The exterior of the cylinder was set to a no-slip condition. Considering the intricate texture of the 3D-printed structure, a roughness parameter with a constant of 0.5 and height of 0.1 mm was implemented at the surface of the POCS. Simulations were conducted with a cold, inert flow of nitrogen set at 293.15 K and 1 atm, replicating experimental conditions. In the heat transfer analysis, a conjugate heat transfer approach was employed, enabling a precise calculation of the POCS surface temperature. In this case, the inlet was assigned a temperature of 400 °C and the external surface of the cylinder had a temperature of 450 °C. The POCS surface's temperature was then governed by heat fluxes and materials properties with Inconel's characteristics being the basis for this study. Additional insights into the physical settings are reported in Appendix A. From the numeric viewpoint, the chosen meshes comprise approximately 4.5 million cells for pressure drop simulations, and around 6 million for thermal simulations, encompassing both the fluid and solid domains. The simulations utilized a pressure-based solver in conjunction with the standard k-ε turbulence model also used in other similar study [22]. Gradient computations were handled using the Least Square Cell-Based discretization scheme, while the Second Order Upwind scheme was

adopted for the discretization of transport properties, including momentum, energy, and turbulence variables. The "coupled" algorithm was chosen for pressure–velocity coupling, ensuring a stable and rapid convergence in this steady-state analysis. Convergence was deemed achieved when the residuals fell below 10^{-4}. A more comprehensive overview of the computational methods, encompassing domain, grid generation, mesh independence analysis and flow development analysis are presented in Appendix B, C and D.

3.2. Performance indicators

The momentum and heat transfer performance are respectively assessed with two indicators namely the pressure drop across the sample and the volumetric heat transfer coefficient often adopted by researchers [42,24]. Pressure drop is defined as the difference between surface average pressure at inlet and outlet, divided by the sample length as per Eq. (3).

$$\frac{\Delta P}{L} = \frac{1}{L}\left(\frac{4}{\pi D^2}\iint p dS_{in} - \frac{4}{\pi D^2}\iint p dS_{out}\right) \qquad 3$$

As expressed in Eq. (4), the volumetric heat coefficient denoted h_v is the product of the surface heat transfer coefficient h ($[W.m^{-2}.K^{-1}]$, defined in Eq. (5), and the specific surface area S_v ($[m^{-1}]$, defined in Eq. (2). This quantity is a relevant performance indicator, as it takes into account both the heat flux, and the contact surface allowed by POCS's geometry

$$h_v = S_v * h \qquad 4$$

$$h = \frac{1}{S_{POCS}}\left(\sum_i \frac{\Phi(i)}{T_{solid}(i) - T_{ref}}\right) \qquad 5$$

Where S_{POCS} is the total area of POCS surface. $\Phi(i)$ is the elementary power exchanged through each i cell's surface adjacent to the solid. T_{solid} (i) is the temperature of each cell i on the solid surface. Within this study's framework, T_{ref} is provisionally defined as the inlet temperature. However, in Section 4.3, it's adjusted to the volume-averaged fluid temperature (cf. Eq. (6), a reference that appears to be more universally accepted [43]. Subsequent comparisons are made with literature based on this adjusted reference.

$$T_{ref} = \frac{1}{V_f}\iiint T dV_f \qquad 6$$

3.3. Engineering correlations

Numerical findings provide the foundation for CFD-driven engineering correlations essential for reactor design. The pressure drop across a porous medium is influenced by its geometrical characteristics, the properties of the working fluid, and its velocity as per Eq. (7).

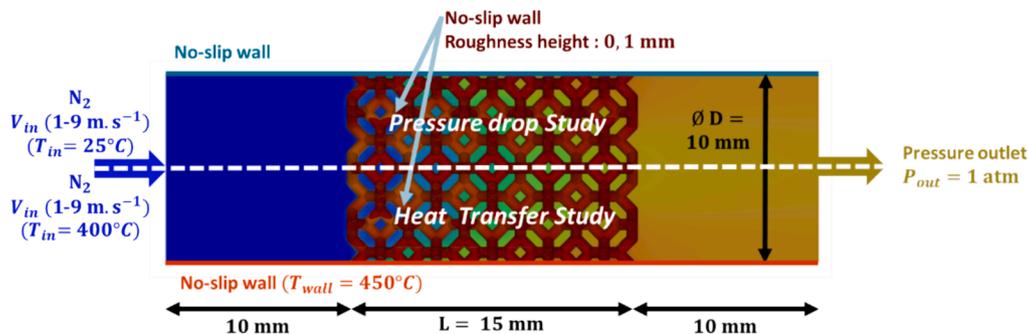$$\frac{\Delta P}{L} = f(\in, L_{char}, \rho, \mu, u) \qquad 7$$

Fig. 2. Implemented boundary conditions and physical setup applied during the pressure drop and heat transfer studies.

The Darcy-Forchheimer equation as presented in Eq. (8) is frequently employed in literature to model pressure drops across porous media and packed beds [44]

$$\frac{\Delta P}{L} = a\boldsymbol{v} + b\boldsymbol{v}^2 \qquad 8$$

This equation accounts for pressure drop in porous media by combining two terms: a viscous component, associated with fluid velocity and viscosity, and an inertial component, related to density and the square of the velocity. The Ergun equation is a standard method utilized by chemical engineers to determine pressure drop in packed beds, often integrated into simplified reactor models. Consistent with prior studies [4], our pressure drop data were regressed using an Ergun-like model, as shown in Eq. (9). In this model, A and B are the Ergun constants representing viscous and inertial terms, respectively. The superficial velocity term in the viscous term has been modified by adding an exponent C to better represent potential nonlinearities. Numerous definitions for characteristic lengths have been proposed, including specific surface area, cell size, and diverse diameters such as strut, hydraulic, or window,
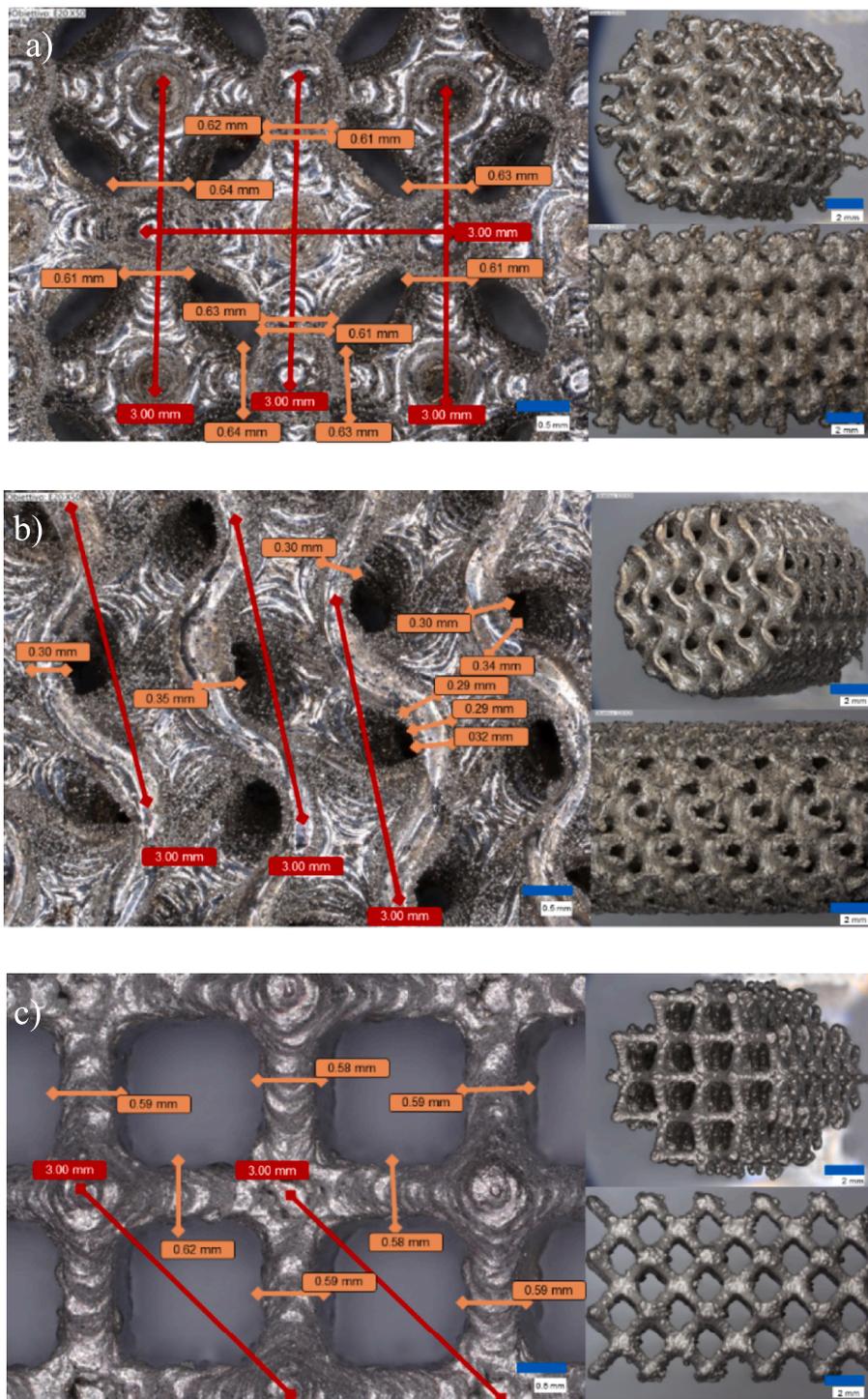
Fig. 3. Macroscopic topography of the sample viewed by digital microscope (a) Kelvin 3–0.6 (measurements: cells 3.0 mm; struts 0.63 mm) (b) BCC 3–0.6 (measurements: cells 3.0 mm; struts 0.59 mm) (c) Gyroid 3–0.3 (measurements: cells 3.03 mm; struts 0.32 mm). All structures presented in this figure are in Ni alloy.
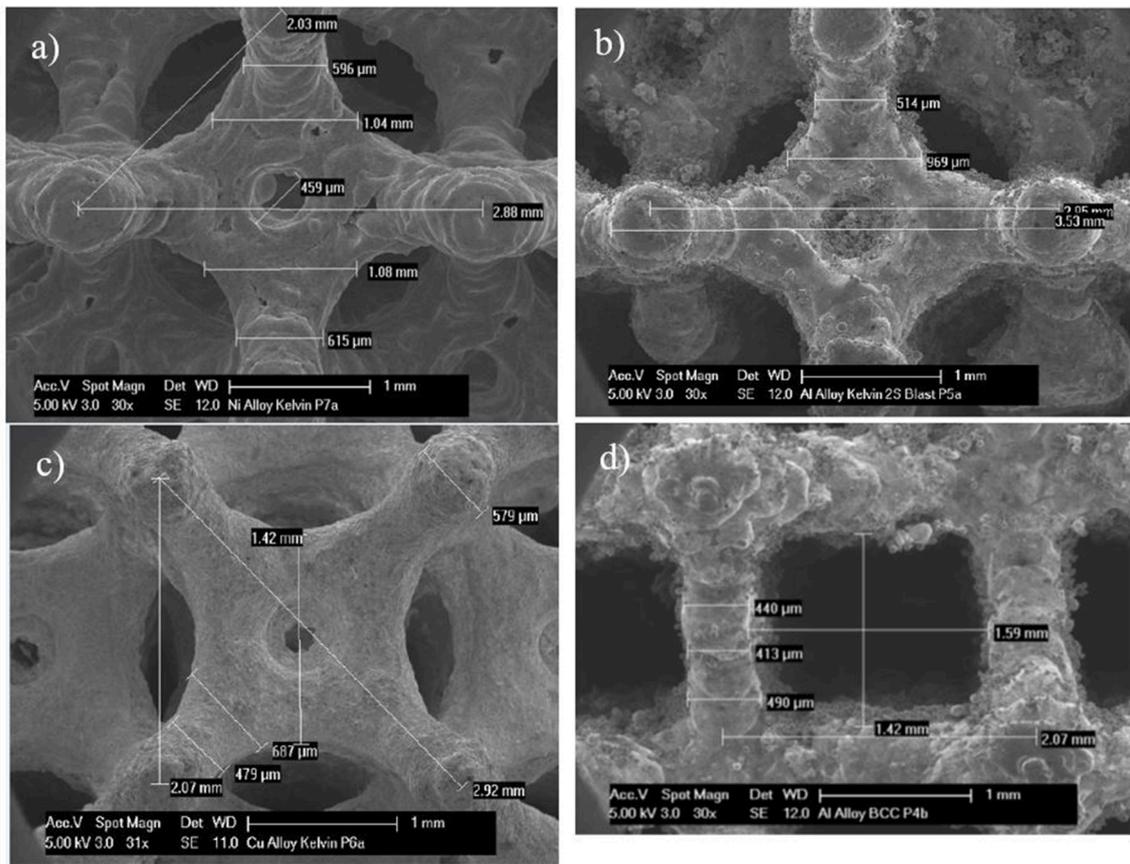
Fig. 4. SEM images of strut surface of cellular structures after the post-processing: Scanning electron microscopy (SEM) micrograph at different magnification of three samples (a) Kelvin 3–0,6 (Ni) (b) Kelvin 3–0,6 (Al)[sb] (c) Kelvin 3–0,6 (Cu)[sb] (d) BCC 3–0,6 (Al alloy).

however a universal standard has yet to be established. For the scope of this study, the strut diameter is chosen for its relevance to catalyst support manufacturability and its straightforward application for engineers:

$$\frac{\Delta P}{L} = \frac{A(1-\epsilon)^C}{\epsilon^3}\frac{\mu v}{d_s^2} + \frac{B(1-\epsilon)}{\epsilon^3}\frac{\rho v^2}{d_s} \qquad 9$$

In this study, MATLAB's lsqcurvefit function was utilized for nonlinear least-squares curve fitting [45]. This tool identifies parameter values by minimizing the squared differences between observed and predicted responses, using the Levenberg-Marquardt algorithm. The performance of the correlation was evaluated using the Mean Absolute Percentage Error (MAPE) and the Root Mean Squared Error (RMSE). MAPE provides a percentage-based insight into prediction errors, while RMSE measures the average magnitude of the error. The equations for MAPE and RMSE can be found in Eq. (10) & Eq. (11), with lower values suggesting a closer fit to the data.

$$MAPE = \frac{100}{N}\sum_{i=1}^{N}\left|\frac{y_{obs,i} - y_{fit,i}}{y_{obs,i}}\right| \qquad 10$$

$$RMSE = \sqrt{\frac{1}{N}\sum_{i=1}^{N}\left(y_{obs,i} - y_{fit,i}\right)^2} \qquad 11$$

4. Result and discussion

4.1. Geometrical characterization

To ensure the accuracy of the 3D printing process, a geometric assessment of the printed replicas was carried out. Fig. 3 illustrates both the front and side perspectives of the sample using varying magnifications with a light microscope. The cell, strut and window diameters were additionally measured at different locations to evaluate the average morphological properties. In general, for the three lattice types, the measurements show that the cell size of the samples matches, on average, the cell size of the CAD while slight deviations can sometimes be noticed regarding strut diameter and window diameters. For example, slight strut thickening can be noticed in proximity of the node convergence. For further details Fig. 4 presents the SEM morphology of different cell surfaces, highlighting variations in textures based on the material used. The AlSi10Mg structure exhibits commonly observed features [10 11] such as partially melted Al alloy particles at the strut surface and a corrugated appearance due to the layer-by-layer additive manufacturing of the LPBF process. On the other hand, nickel and copper alloy samples exhibit a smoother surface. In case of Ni alloy, this could be due to optimized process parameter regarding the surface roughness and for the Cu alloy, it can directly be attributed to the sand-blasting process that removed the satellite particles from the surface. Finally, as observed in Fig. 5, pycnometry experiments reveal that the porosity of the printed design is less than the one predicted by the CAD
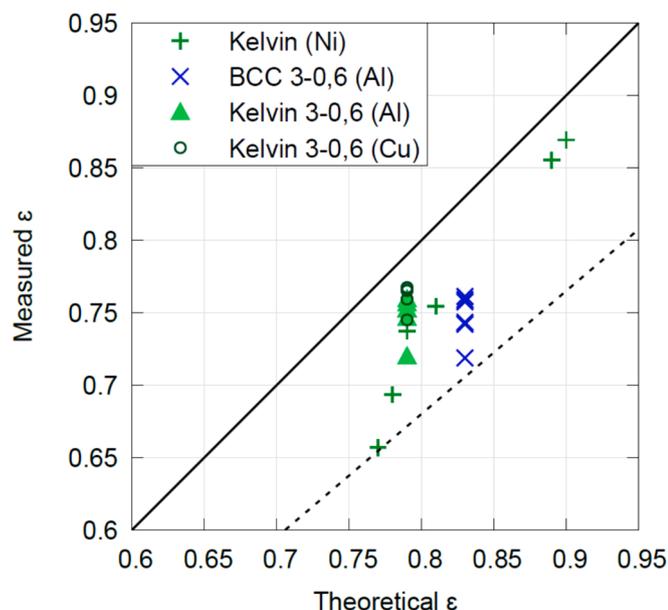
Fig. 5. Experimental hydrodynamic porosity measured with pycnometry compared to the theoretical (CAD) porosity. The 15% error margin is indicated by a dashed line.

value file, with discrepancies reaching up to 15 %. This is in line with deviation observed in the literature [31]. Such variations are particularly pronounced for the cell design with the finest details, like the Kelvin's square window at low porosity.

4.2. Pressure drop investigation

In this section, the outcomes of the CFD simulations are explored. First the accuracy of pressure drop predictions is verified against experimental results, and then the selected POCS designs are compared based on their specific surface area and porosity. Fig. 6 presents a comparison of pressure drop trends across velocities, contrasting experimental and simulation data for the chosen cell types. The shaded region for the BCC structure encompasses results from two experimental datasets: BCC 3-0.6 in both Al alloy and Ni alloy. In the case of the Kelvin cell 3-0.6, the shaded area includes readings from three different measurements: namely Al alloy, Cu alloy (both sandblasted), and Ni alloy. The shaded curve gives an average variability of 22 %, indicative of standard deviation across experiments. Such variations underline inherent differences across materials studied. Pressure drops obtained at high velocity (≥ 5 m.s^{-1}) from CFD simulations align remarkably well within the experimental variability range. On the other hand, at slower velocities, there is an inclination towards over-predicting the pressure drop. This difference is especially notable for BCC 3-0.6, showing a deviation of up to 67 % at 2 m.s^{-1}. Such variances may be rooted in turbulent flow modelling nuances, given the pronounced laminar tendencies at these speeds. Overall, a reasonable agreement is obtained between numerical and experimental data. To discern the cell type's
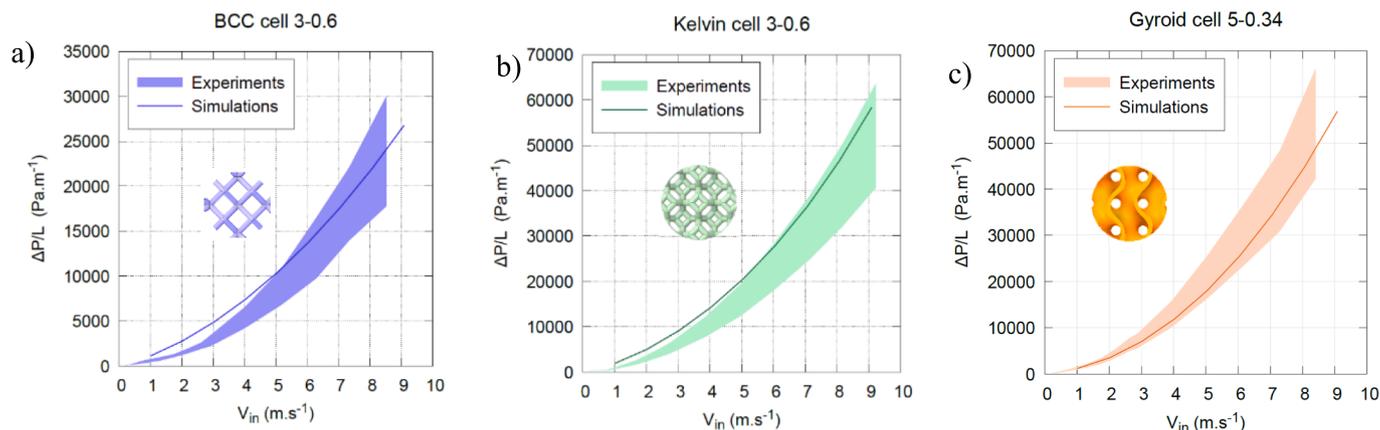

Fig. 6. Experimental validation of our CFD settings (a) BCC (b) Kelvin (c) Gyroid.
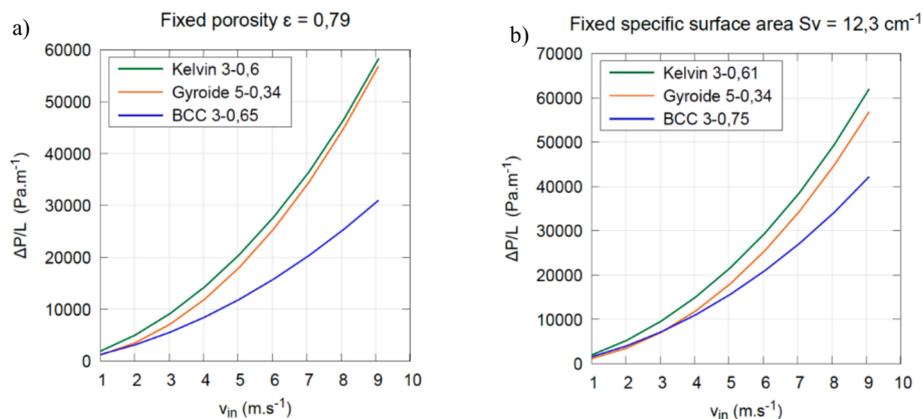

Fig. 7. Pressure drop comparison on various structures, with fixed geometrical parameters (a) fixed porosity (b) fixed specific surface area (Reynolds number varies from 38 to 348 for Kelvin and BCC lattices, and from 22 to 254 for the Gyroid lattice).
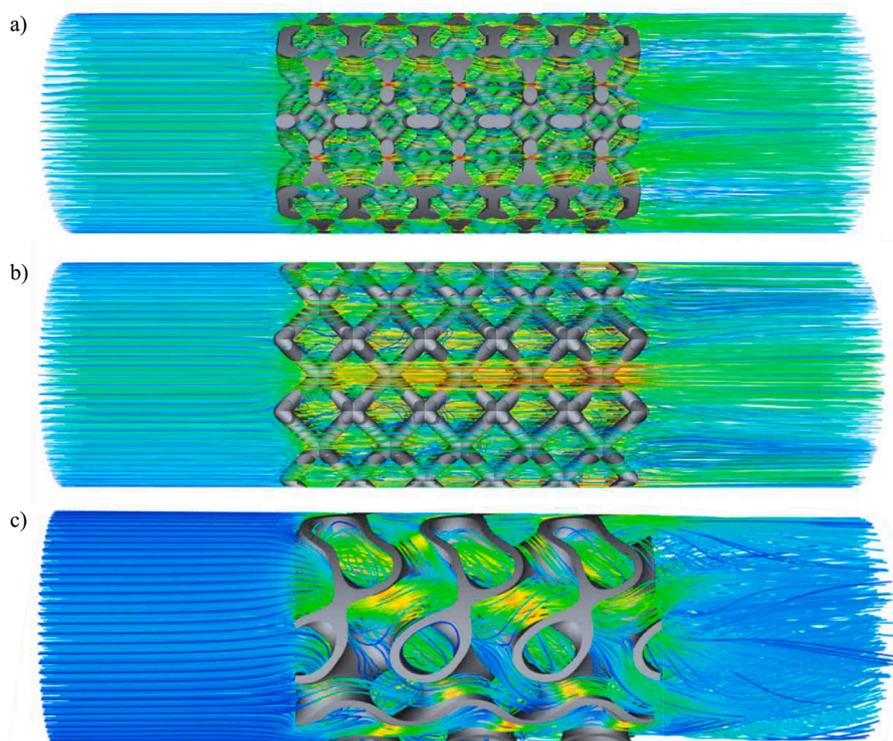
Fig. 8. Streamline visualization across (a) Kelvin (b) BCC (c) Gyroid lattices.

influence on pressure drop, distinct structures, all maintaining a similar porosity ($\epsilon = 0,79$) and specific surface area ($S_v = 12,3$ cm^{-1}). The results are reported in Fig. 7. Interestingly, the Kelvin structure consistently registered the most pronounced pressure drop, followed closely by the Gyroid (showing only a 3 % differential at 9 m.s^{-1} with a constant porosity). Conversely, BCC showcased the least pressure drop, behind the Kelvin by 47 % at 9 m.s^{-1} under similar porosity. Such distinctions can be attributed to the unique designs of the cells: as observed in Fig. 8, the Kelvin structure, with its square openings oriented perpendicularly to the flow, creates flow constrictions that add considerable resistance, especially in the inertial regime. This design induces a more energy-intensive flow pattern within the matrix, amplifying energy dissipation, as supported by related studies [36 32]. Conversely, the gyroid lattice's streamlines depict a highly tortuous path also leading to increased friction and, thus, a higher pressure drop. Meanwhile, the BCC structure provides a relatively unimpeded flow. When evaluating solely on the basis of pressure drop, the BCC design is notably superior.

4.3. Heat transfer investigation

While pressure drop is an important metric, it's just one piece of the puzzle. As many industrial applications involve significant heat transfer, it is essential to consider both pressure drop and heat transfer characteristics for a more holistic evaluation of the POCS. As stated in Section 3.2. The volumetric heat transfer coefficient, denoted h_v (using the inlet temperature as the reference temperature) is the metric used to rank the structures. It can be seen in Fig. 9 that Kelvin cell consistently presents the highest value. At fixed specific surface area the BCC trails behind the Kelvin cell (18 % deficit) but still surpasses the Gyroid structure by a margin of 6 %. At fixed porosity, it is intriguing to note that the distinction between BCC and Gyroid is very light making them almost analogous. Considering the aim to achieve the highest possible h_v, the Kelvin cell distinctly stands out as the best choice from the heat transfer viewpoint.
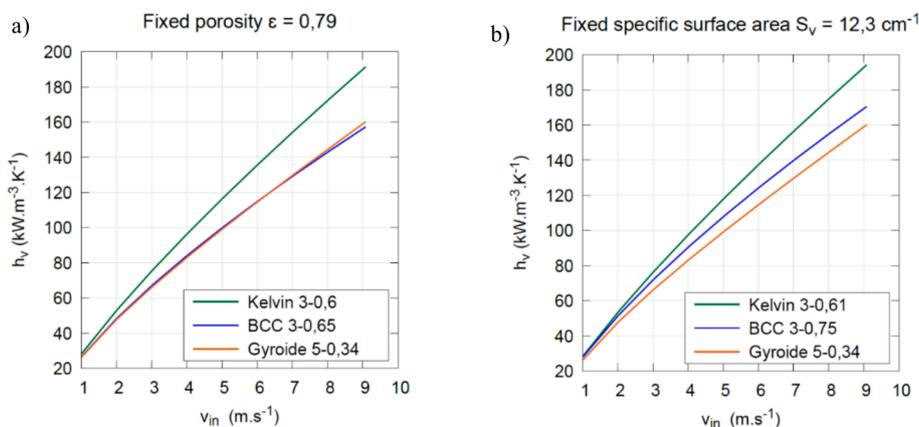

Fig. 9. Volumetric heat transfer coefficient on various structures with fixed geometrical parameters (a) fixed porosity (b) fixed specific surface area.
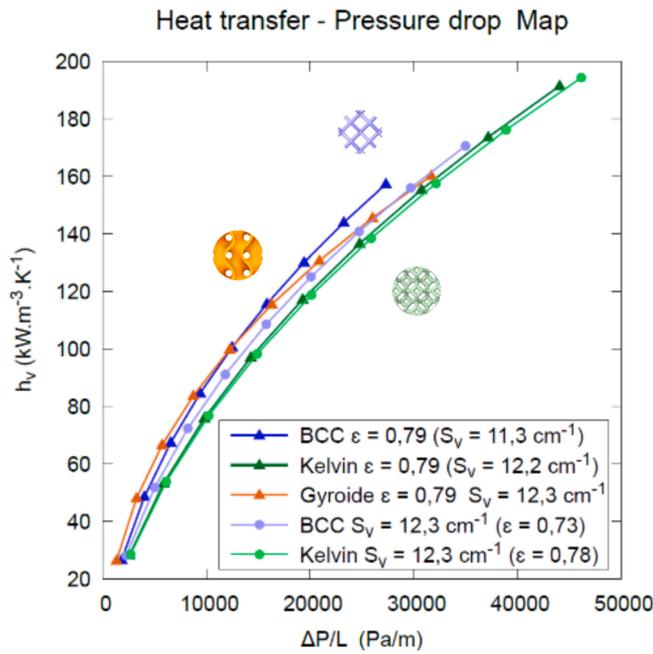
Fig. 10. Heat transfer − pressure drop map.

4.4. Trade off heat transfer-pressure drop

In evaluating optimal structural design, a balance between pressure drop and heat transfer is essential. Based on insights from prior sections, this section aims to identify the structure that offers minimal pressure drop while ensuring maximum volumetric heat transfer coefficient. A h_v − $\Delta P/L$ graph is therefore plotted on Fig. 10. Although the performance between structures is fairly similar, a ranking can still be determined. When maintaining constant porosity, the Gyroid curve remains dominant until reaching a specific velocity, at which point the BCC becomes preferable. Yet, by extrapolating the current trends, the Kelvin cell could outperform the Gyroid when h_v exceeds 170 kW.m^{-3}.K^{-1}.

4.5. Engineering correlations & comparison with literature

An Ergun-type correlation, as detailed in Eq. (9) in section 3.3 is fitted to our CFD data to represent the pressure drop across our selected lattices. Fig. 11 presents the respective parity plots comparing the correlation predictions with the CFD simulation outcomes. Regression analysis constants, as well as the MAPE and RMSE values, are reported in Table 3. The results exhibit a good alignment, with a MAPE of less than 10 %. For comparison with the literature, and given the absence of known existing correlations for the BCC and Gyroid lattices, our results are compared with established correlations obtained for the Kelvin cell lattice as display in Fig. 11(a). The correlation of Ferroni et al. (2022) [31] is found to slightly overestimate our data with a MAPE of 18 %, while Rambabu et al. (2021) [33] do so with a MAPE of 25 %. Excluding data points with the lowest porosity value reduces the MAPE to 12 %, implying that their correlation might not perform as well with lower porosities. The correlation of Bracconi et al. (2019) [4] derived from virtually generated OCF, yields a MAPE of 19.62 %. On the whole, pressure drop results obtained in this study appear to be in quite good agreement with literature. Additionally, the simple correlations derived in this work, based on readily accessible parameters like strut size or gyroid thickness, could assist in reactor design endeavors and also serve as a reference for comparison in subsequent research in this field. For the heat transfer analysis, comparisons of our results with established literature correlations are presented in Fig. 12, utilizing the conventional heat transfer coefficient h. As explained in Section 3.2, the heat
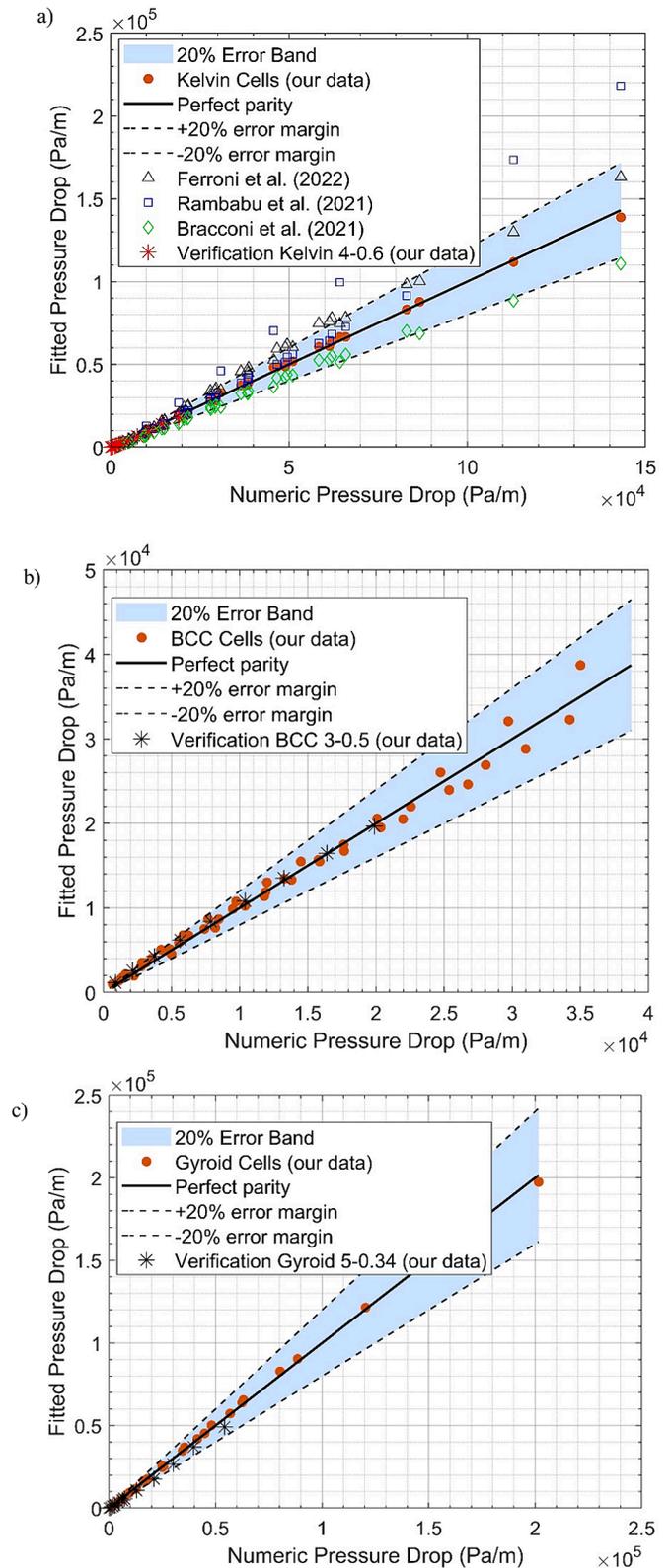

Fig. 11. Parity plots comparing pressure drop obtained by the numeric investigation and correlation predictions for our selected POCS samples (a) Kelvin (b) BCC (c) Gyroid with the 20% error margin band. The star markers in each plot indicate the verification points used to check the proposed correlations.

Table 3

Constants for the proposed pressure drop correlation as defined in Eq. (9) for the three lattices (presumed Reynolds validity range: $30 < Re_{ds} < 400$).

	Kelvin	BCC	Gyroid
Porosity validity interval	$0.66 < \epsilon < 0.8$	$0.72 < \epsilon < 0.92$	$0.7 < \epsilon < 0.8$
Fitted A	999.6348	83.5654	37260.0992
Fitted B	0.82099	0.26672	0.48628
Fitted C	3.4497	1.0837	9.818
RMSE (Pa/m)	1359.139	775.2997	1354.1546
MAPE (%)	9.0678	9.0718	6.5898

transfer coefficient is recalculated using the volume-averaged fluid temperature as the reference, resulting in a higher value − a definition somewhat more adopted [32]. Nonetheless, there is a noticeable variation in heat transfer coefficient estimates. This variation could stem from several factors in numerical simulations: differing boundary conditions like constant wall heat flux versus constant wall temperature; the choice between conjugate heat transfer or a set thermal boundary in some research; the role of operating conditions and specific characteristics of the working fluid; and potential differences in methodologies for calculating the heat transfer coefficient across studies. Overall, the values predicted in this study align reasonably with literature data, albeit rather towards the lower end.

5. Conclusions

This study conducted an in-depth comparative analysis of three POCS: the widely recognized Kelvin cell, and the lesser-known BCC and gyroid lattice. Through a blend of numerical and experimental approaches, the study emphasized the design and fabrication using Laser Powder Bed Fusion, as well as the analysis of these structures using CFD simulations.

(1) Regarding the manufacturability, various physico-morphological characterization techniques were utilized to determine geometric characteristics of 3D printed samples. The printed samples closely resembled their CAD counterparts, with an observed porosity deviating by a maximum of 15 % less than the intended design values.

(2) A CFD model was validated based on pressure drop experimental campaign and subsequently employed to conduct an in-depth comparison of POCS based on shared geometric features, specifically porosity and specific surface area. In terms of pressure drop, the BCC stands out as the superior structure. In contrast, the Kelvin cell registered the highest performance among all configurations from a heat transfer perspective. While the performance of the structures is relatively comparable, Gyroid configurations seem to offer superior momentum and heat transfer characteristics at lower velocities region whereas the BCC structure demonstrates superiority in the high-velocity range.

(3) An Ergun-like correlation was formulated and validated for all three cell types, achieving a MAPE of less than 10 %. When compared with existing literature correlations, our results demonstrated good alignment too, with a MAPE of less than 20 %. Concerning heat transfer, the values forecasted in this research show a reasonable alignment with literature figures, though they tend to be on the lower spectrum.

This study advances our understanding of POCS thermohydraulic properties, offering insights for selecting cell types and also scaling up reactors or other continuous flow systems utilizing these structures, yet several areas remain unexplored. For example, a comprehensive analysis should also factor chemical reactions, moreover, many POCS designs have yet to be investigated, and cell orientation might have a significant impact, particularly in the gyroid lattice.

CRediT authorship contribution statement

S. Richard: Writing – review & editing, Writing – original draft, Visualization, Validation, Software, Project administration, Methodology, Investigation, Formal analysis, Data curation, Conceptualization. **D. Tasso:** Writing – review & editing, Visualization, Validation,
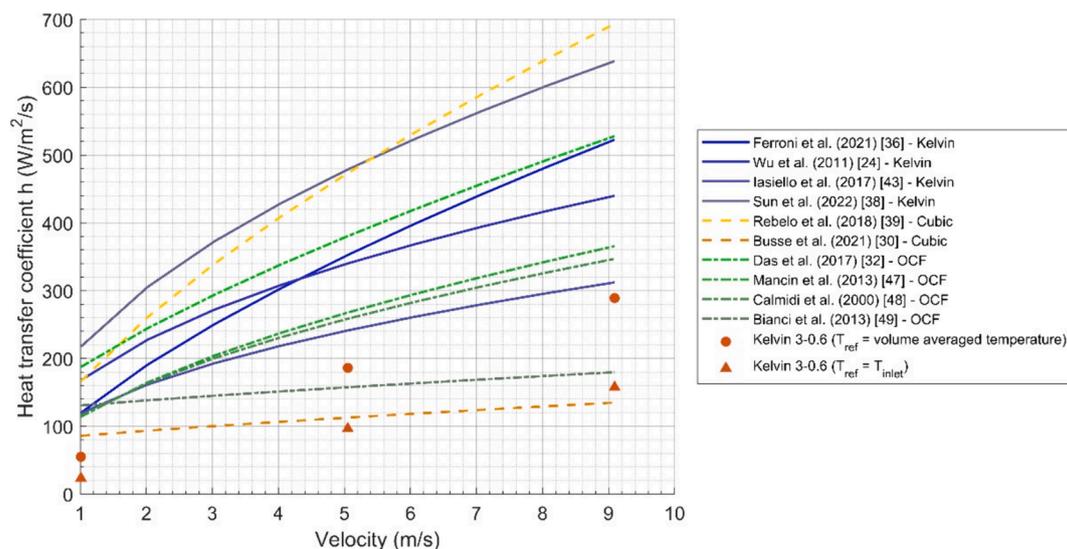
Fig. 12. Comparison of our data with correlations found in the literature (Kelvin [36 24 46 38] Cubic [39 30] and OCF [32 47 48 49]). The dot and triangle markers refer to the numerical results obtained using two different methodologies.

Declaration of competing interest

Data availability

Acknowledgement

Appendix A:. Physical setting details

Table 4
Recap of physical settings for pressure drop simulations.

Name	Value
Operating temperature	$25°$ C
Operating pressure	1atm
Inlet velocity	$\{1, 2, 3, \cdots, 9\}$m.s^{-1}
Fluid density	$1,1452$kg.m^{-3}[9]
Fluid viscosity	$1,7805.10^{-5}$ Pl[9]

Table 5
Recap of physical settings for pressure drop simulations.

Name	Symbol	Value
Inlet temperature	T_{in}	$400°$ C
Wall temperature	T_{wall}	$450°$ C
Operating pressure	P_{op}	1atm
Inlet velocity	v_{in}	$\{1, 2, 3, 4, 5, 6, 7, 8, 9\}$ m.s^{-1}
Solid density	$\rho(\text{in}625)$	8440kg.m^{-3}
Solid specific heat	$C_p(\text{in}625)$	Piecewise-linear, taken from [10] (500J.kg^{-1}.K^{-1})
Solid thermal conductivity	$\lambda(\text{in}625)$	Piecewise-linear, taken from [10] (17W.m^{-1}.K^{-1})
Fluid density	$\rho(\text{N}_2)$	Computed (Fluent "incompressible-ideal-gas")
Fluid specific heat	$C_p(\text{N}_2)$	Variable (Fluent "nasa-9-piecewise-polynomial") (1100J.kg^{-1}.K^{-1})
Fluid thermal conductivity	$\lambda(\text{N}_2)$	Piecewise-linear, taken from [9] ($0,05$W.m^{-1}.K^{-1})
Fluid viscosity	$\mu(\text{N}_2)$	Computed (Fluent "kinetic-theory")

Appendix B:. Mesh convergence analysis

A mesh convergence analysis was carried out aiming at obtaining pressure drop results independent of the grid refinement in the numerical investigation. For each of the three different types of structure, we made a meshing convergence study. Five meshes were tested for Kelvin and BCC structures, and four for Gyroid. For each of them, we made simulations corresponding to the nine flow speeds from 1 to 9 m.s^{-1}. We then measured the pressure drop obtained and compared them to the value achieved with the finest mesh. Results are shown on Figure 13, on which each point represents the average error of the nine speeds Considering the results of the convergence study, for each structure we retained the meshes with about 4,5M cells, as they allow about 1 % error and good computation time. Table 6 gives the typical settings we used to generate meshes with this number of cells. We used these parameters for all the other structures, including those for thermal simulations.

Fig. 13. Mesh sensitivity.

Table 6
Typical mesh generation settings.

Setting	Value
Surface local sizing	0,05 mm on POCS surface
General minimum surface size	0,1 mm
Maximum surface size	0,4 mm
Surface growth rate	1,2
Boundary smooth transition	Layers: 3, Transition ratio: 0,272, Growth rate: 1,2
Maximum cell length	0,4 mm
Volume growth rate	1,2

Appendix C:. Ansys Fluent Solver setting

Table 7
Ansys Fluent Solver settings.

Setting	Value
Time	Steady-state
Solver type	Pressure-based
Pressure-velocity scheme	Coupled
Gradient discretization	Least squares cell based
Spatial discretization	Second order (upwind)
Pseudo-time method	Global time step
Viscous model	k- ε realizable, with scalable wall functions
Maximum tolerated continuity residual (with all other residuals lower)	10^{-4}

Appendix D:. Analysis of flow development

To investigate the effects of the POCS inlet and outlet on pressure drop, fresh simulations were conducted using the BCC 3–0.6 geometry. Considering the phenomenon's non-linear nature, the study included simulations on both a standard-length sample (15 mm) and a 1.4-times elongated sample (21 mm), with airflows set at 1 and 9 m/s. The actual values for the elongated sample were then compared to the extrapolated values from the standard sample, which were adjusted by the 1.4 factor. The results are presented in Table 8 below: As the gap is only 1 % between elongated sample and proportional value from standard sample, inlet and outlet effects can be considered as negligible. A length of 15 mm is found sufficient for

achieving a fully developed flow. Specifically, at an inlet speed of 9 m/s (the maximum speed, at which the flow requires the longest distance to fully develop), the velocity field exhibits periodic behavior in accordance with the geometry. As depicted in Fig. 14, for two adjacent cutting planes with an inlet speed of 9 m/s, the velocity field is consistently repeated from the second cell in the flow direction, confirming that the flow stabilizes after about 6 mm. This observation underscores the establishment of a fully developed flow pattern.

Table 8
Effect of POCS sample length on pressure drop.

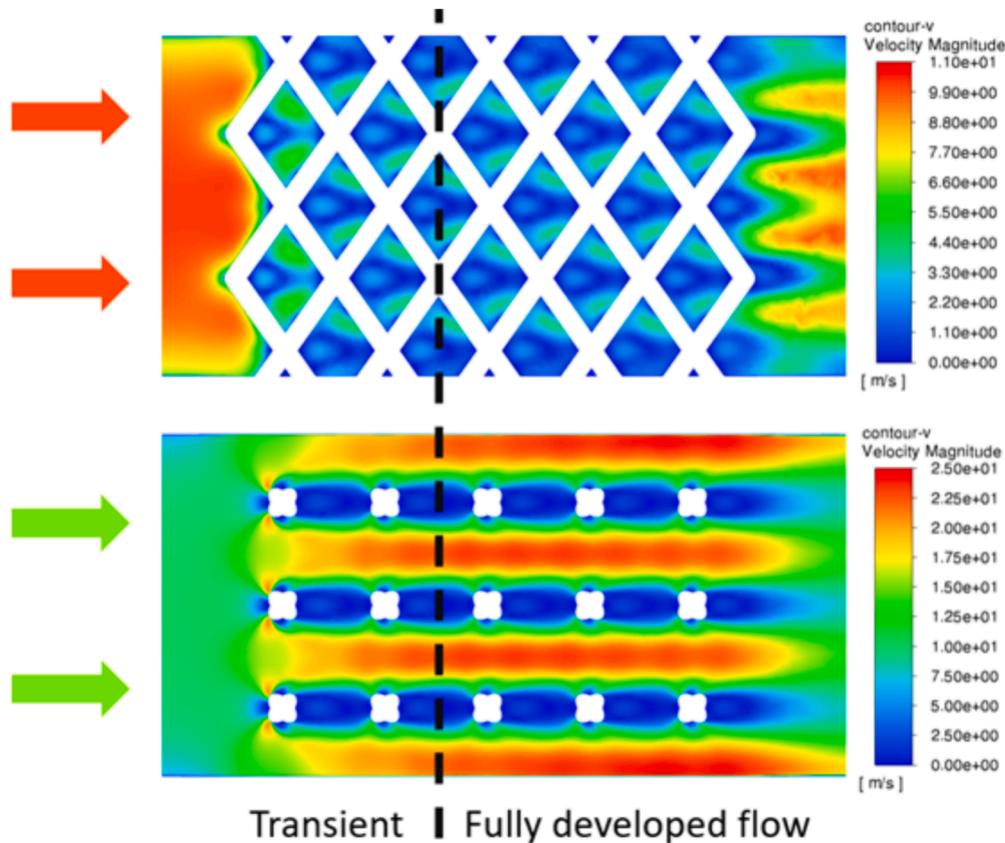| Vin (m/s)	Pressure drop $\Delta P/L$ (Pa/m) Standard sample length (15 mm)	Extrapolated value for elongated sample (* 1.4 factor)	Real value for elongated sample (* 1.4 factor)	Relative gap (Proportional – Real values)
1	1 115	1 561	1 564	0,2 %
9	26 749	37 448	36 976	1,3 %

Fig. 14. Analysis of Flow Development on BCC 3–0.6 for two adjacent cutting planes.

Appendix E:. Turbulence model justification

For flow through homogeneous porous media, for very low fluid velocity, the pressure drop is only balanced by the viscous shear stress at the solid surfaces (Darcy regime). When the Reynolds number is gradually increased, in the Forchheimer regime, the inertial forces related to the local acceleration of the fluid particles starts contributing and the total pressure drop contains both viscous and inertial contributions. The exact limiting value of the Reynolds number for flow transition from Darcy regime to Forchheimer regime depends on the structure of the porous medium. The study of Das et al. (2017) [32] offers insight into the transition Reynolds number, using DNS on a Kelvin cell study, as depicted in Figure 15. In our operating condition, we predominantly observe the Forchheimer regime, suggesting that both laminar and RANS simulation could be suitable alternatives. In our study the choice is made to resort to RANS simulation to cover the full velocity range.
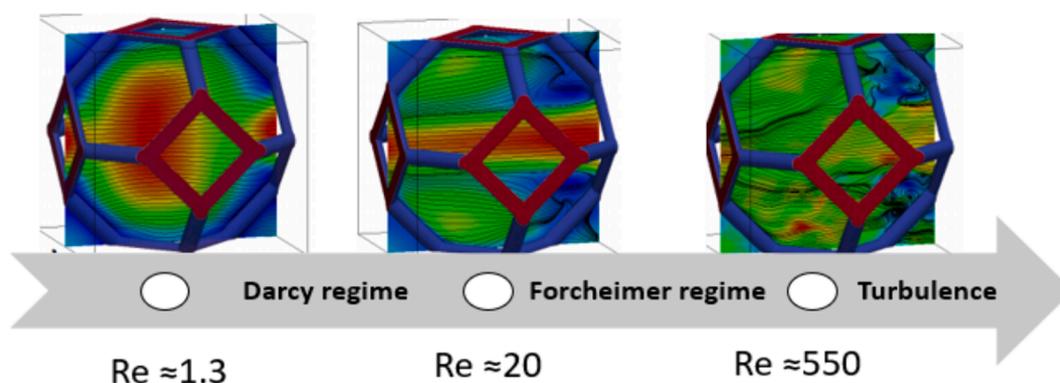
Fig. 15. Description of the hydrodynamic regimes based on an equivalent sphere diameter as a characteristic length scale adapted from Das et al. (2017) [32].

References

[1] F. Kapteijn, J.A. Moulijn, Structured catalysts and reactors – perspectives for demanding applications, Catal. Today 383 (2022) 5–14, https://doi.org/10.1016/j.cattod.2020.09.026.

[2] H.J. Venvik, J. Yang, Catalysis in microstructured reactors: Short review on small-scale syngas production and further conversion into methanol, DME and Fischer-Tropsch products, Catal. Today 285 (2017) 135–146, https://doi.org/10.1016/j.cattod.2017.02.014.

[3] L.C. Almeida, O. Sanz, D. Merino, G. Arzamendi, L.M. Gandía, M. Montes, Kinetic analysis and microstructured reactors modeling for the Fischer-Tropsch synthesis over a Co–Re/Al2O3 catalyst, Catal. Today 215 (2013) 103–111, https://doi.org/10.1016/j.cattod.2013.04.021.

[4] M. Bracconi, M. Ambrosetti, O. Okafor, V. Sans, X. Zhang, X. Ou, C.P. Da Fonte, X. Fan, M. Maestri, G. Groppi, E. Tronconi, Investigation of pressure drop in 3D replicated open-cell foams: Coupling CFD with experimental data on additively manufactured foams, Chem. Eng. J. 377 (2019) 120123, https://doi.org/10.1016/j.cej.2018.10.060.

[5] M. Iwaniszyn, Periodic Open Cellular Structures (POCS) as catalyst supports—a review, Energies 15 (2022) 7703, https://doi.org/10.3390/en15207703.

[6] C. Parra-Cabrera, C. Achille, S. Kuhn, R. Ameloot, 3D printing in chemical engineering and catalytic technology: structured catalysts, mixers and reactors, Chem. Soc. Rev. 47 (2018) 209–230, https://doi.org/10.1039/C7CS00631D.

[7] Y. Zhang, Additive manufacturing of metallic materials: a review, J. Mater. Eng. Perform. (n.d.) 13.

[8] S. Danaci, Optimisation et integration de catalyseurs structurés pour la conversion de CO2 en methane, Université Grenoble Alpes, 2017.

[9] M. Klumpp, A. Inayat, J. Schwerdtfeger, C. Körner, R.F. Singer, H. Freund, W. Schwieger, Periodic open cellular structures with ideal cubic cell geometry: Effect of porosity and cell orientation on pressure drop behavior, Chem. Eng. J. 242 (2014) 364–378, https://doi.org/10.1016/j.cej.2013.12.060.

[10] Z. Li, Y. Nie, B. Liu, Z. Kuai, M. Zhao, F. Liu, Mechanical properties of AlSi10Mg lattice structures fabricated by selective laser melting, Mater. Des. 192 (2020) 108709, https://doi.org/10.1016/j.matdes.2020.108709.

[11] C. Yan, L. Hao, A. Hussein, D. Raymont, Evaluations of cellular lattice structures manufactured using selective laser melting, Int J Mach Tool Manu 62 (2012) 32–38, https://doi.org/10.1016/j.ijmachtools.2012.06.002.

[12] R. Balzarotti, A. Bisaccia, M.C. Tripi, M. Ambrosetti, G. Groppi, E. Tronconi, Production and characterization of copper periodic open cellular structures made by 3D printing-replica technique, Jnl Adv Manuf Process 2 (2020), https://doi.org/10.1002/amp2.10068.

[13] T. Horneber, Thermo-fluid dynamic characterization and technical optimization of structured open-cell metl foam by means of numerical simulation, Friedrich Alexander Universitat Erlangen Nurnberg, 2015.

[14] S. Meinicke, K. Dubil, T. Wetzel, B. Dietrich, Characterization of heat transfer in consolidated, highly porous media using a hybrid-scale CFD approach, Int. J. Heat Mass Transf. 149 (2020) 119201, https://doi.org/10.1016/j.ijheatmasstransfer.2019.119201.

[15] M. Lämmermann, G. Horak, W. Schwieger, H. Freund, Periodic open cellular structures (POCS) for intensification of multiphase reactors: Liquid holdup and two-phase pressure drop, Chem. Eng. Process. - Process Intesif. 126 (2018) 178–189, https://doi.org/10.1016/j.cep.2018.02.027.

[16] A. Chaudhari, P. Ekade, S. Krishnan, Experimental investigation of heat transfer and fluid flow in octet-truss lattice geometry, Int. J. Therm. Sci. 143 (2019) 64–75, https://doi.org/10.1016/j.ijthermalsci.2019.05.003.

[17] F.M. Baena-Moreno, M. González-Castaño, J.C. Navarro de Miguel, K.U.M. Miah, R. Ossenbrink, J.A. Odriozola, H. Arellano-García, Stepping toward efficient microreactors for CO2 methanation: 3D-Printed gyroid geometry, ACS Sustain. Chem. Eng. 9 (2021) 8198–8206, https://doi.org/10.1021/acssuschemeng.1c01980.

[18] Z. Cheng, R. Xu, P.-X. Jiang, Morphology, flow and heat transfer in triply periodic minimal surface based porous structures, Int. J. Heat Mass Transf. 170 (2021) 120902, https://doi.org/10.1016/j.ijheatmasstransfer.2021.120902.

[19] Z. Ahmed Qureshi, S. Addin Burhan Al-Omari, E. Elnajjar, O. Al-Ketan, R. Abu Al-Rub, Architected lattices embedded with phase change materials for thermal management of high-power electronics: a numerical study, Appl. Therm. Eng. 219 (2023) 119420, https://doi.org/10.1016/j.applthermaleng.2022.119420.

[20] Z.A. Qureshi, S. Addin Burhan Al-Omari, E. Elnajjar, O. Al-Ketan, R.A. Al-Rub, On the effect of porosity and functional grading of 3D printable triply periodic minimal surface (TPMS) based architected lattices embedded with a phase change material, Int. J. Heat Mass Transf. 183 (2022) 122111, https://doi.org/10.1016/j.ijheatmasstransfer.2021.122111.

[21] T. Zheng, W. Zhou, D. Geng, Y. Li, Y. Liu, C. Zhang, Methanol steam reforming microreactor with novel 3D-Printed porous stainless steel support as catalyst support, Int. J. Hydrogen Energy 45 (2020) 14006–14016, https://doi.org/10.1016/j.ijhydene.2020.03.103.

[22] Y. Tang, H. Wang, C. Huang, Pore-scale numerical simulation of the heat transfer and fluid flow characteristics in metal foam under high Reynolds numbers based on tetrakaidecahedron model, Int. J. Therm. Sci. 184 (2023) 107903, https://doi.org/10.1016/j.ijthermalsci.2022.107903.

[23] J.E.V. Rickenbach, Multi-scale modeling of catalytic reactions in open cell foams, ETH Zurich (2015), https://doi.org/10.3929/ETHZ-A-010483809.

[24] Z. Wu, C. Caliot, G. Flamant, Z. Wang, Numerical simulation of convective heat transfer between air flow and ceramic foams to optimise volumetric solar air receiver performances, Int. J. Heat Mass Transf. 54 (2011) 1527–1537, https://doi.org/10.1016/j.ijheatmasstransfer.2010.11.037.

[25] H. Lu, L. Yang, Z. Wu, S. Xu, Numerical and experimental study on convective heat transfer characteristics in foam materials, Energies 13 (2020) 348, https://doi.org/10.3390/en13020348.

[26] I. Kaur, P. Singh, Flow and thermal transport through unit cell topologies of cubic and octahedron families, Int. J. Heat Mass Transf. 158 (2020) 119784, https://doi.org/10.1016/j.ijheatmasstransfer.2020.119784.

[27] S. Cunsolo, M. Iasiello, M. Oliviero, N. Bianco, W.K.S. Chiu, V. Naso, Lord kelvin and weaire-phelan foam models: heat transfer and pressure drop, J. Heat Transfer 138 (2016) 022601, https://doi.org/10.1115/1.4031700.

[28] F. Lucci, A. Della Torre, G. Montenegro, P. Dimopoulos Eggenschwiler, On the catalytic performance of open cell structures versus honeycombs, Chem. Eng. J. 264 (2015) 514–521, https://doi.org/10.1016/j.cej.2014.11.080.

[29] I. Lucentini, G. García Colli, C. Luzi, I. Serrano, L. Soler, N.J. Divins, O.M. Martínez, J. Llorca, Modelling and simulation of catalytic ammonia decomposition over Ni-Ru deposited on 3D-printed CeO2, Chem. Eng. J. 427 (2022) 131756, https://doi.org/10.1016/j.cej.2021.131756.

[30] C. Busse, H. Freund, W. Schwieger, Intensification of heat transfer in catalytic reactors by additively manufactured periodic open cellular structures (POCS), Chem. Eng. Process. - Process Intesif. 124 (2018) 199–214, https://doi.org/10.1016/j.cep.2018.01.023.

[31] C. Ferroni, F.S. Franchi, M. Ambrosetti, M. Bracconi, G. Groppi, M. Maestri, E. Tronconi, Numerical and experimental investigation of pressure drop in periodic open cellular structures for intensification of catalytic processes, ACS Eng. Au (2022), https://doi.org/10.1021/acsengineeringau.1c00034.

[32] Das, S., Transport through bidisperse porous media, TU eindhoven, 2017.

[33] S. Rambabu, K. Kartik Sriram, S. Chamarthy, P. Parthasarathy, V. Ratna kishore, A proposal for a correlation to calculate pressure drop in reticulated porous media with the help of numerical investigation of pressure drop in ideal & randomized reticulated structures, Chem. Eng. Sci. 237 (2021) 116518, https://doi.org/10.1016/j.ces.2021.116518.

[34] F. Lucci, A. Della Torre, G. Montenegro, R. Kaufmann, P. Dimopoulos Eggenschwiler, Comparison of geometrical, momentum and mass transfer characteristics of real foams to Kelvin cell lattices for catalyst applications, Int. J. Heat Mass Transf. 108 (2017) 341–350, https://doi.org/10.1016/j.ijheatmasstransfer.2016.11.073.

[35] M. Sun, M. Li, C. Hu, L. Yang, Y. Song, D. Tang, J. Zhao, Comparison of forced convective heat transfer between pillar and real foam structure under high Reynolds number, Appl. Therm. Eng. 182 (2021) 116130, https://doi.org/10.1016/j.applthermaleng.2020.116130.

[36] C. Ferroni, M. Bracconi, M. Ambrosetti, M. Maestri, G. Groppi, E. Tronconi, A fundamental investigation of gas/solid heat and mass transfer in structured catalysts based on periodic open cellular structures (POCS), Ind. Eng. Chem. Res. 60 (2021) 10522–10538, https://doi.org/10.1021/acs.iecr.1c00215.

[37] C. Moon, H.D. Kim, K.C. Kim, Kelvin-cell-based metal foam heat exchanger with elliptical struts for low energy consumption, Appl. Therm. Eng. 144 (2018) 540–550, https://doi.org/10.1016/j.applthermaleng.2018.07.110.

[38] M. Sun, G. Yan, M. Ning, C. Hu, J. Zhao, F. Duan, D. Tang, Y. Song, Forced convection heat transfer: a comparison between open-cell metal foams and additive manufactured kelvin cells, Int. Commun. Heat Mass Transfer 138 (2022) 106407, https://doi.org/10.1016/j.icheatmasstransfer.2022.106407.

[39] N.F.B. Rebelo, Pressure drop and heat transfer properties of cubic iso-reticular foams, Chem. Eng. 7 (2018).

[40] G. Do, M. Geißelbrecht, W. Schwieger, H. Freund, Additive manufacturing of interpenetrating periodic open cellular structures (interPOCS) with in operando adjustable flow characteristics, Chem. Eng. Process. - Process Intesif. 148 (2020) 107786, https://doi.org/10.1016/j.cep.2019.107786.

[41] I.R. Woodward, L. Attia, P. Patel, C.A. Fromen, Scalable 3D printed lattices for pressure control in fluid applications, AIChE J 67 (2021) e17452.

[42] S. Xu, Z. Wu, H. Lu, L. Yang, Experimental study of the convective heat transfer and local thermal equilibrium in ceramic foam, Processes 8 (2020) 1490, https://doi.org/10.3390/pr8111490.

[43] M. Iasiello, N. Bianco, W.K.S. Chiu, V. Naso, Anisotropic convective heat transfer in open-cell metal foams: assessment and correlations, Int. J. Heat Mass Transf. 154 (2020) 119682, https://doi.org/10.1016/j.ijheatmasstransfer.2020.119682.

[44] C. Italiano, M.A. Ashraf, L. Pino, C.W.M. Quintero, S. Specchia, A. Vita, Rh/CeO$_2$ thin catalytic layer deposition on alumina foams: catalytic performance and controlling regimes in biogas reforming processes, Catalysts 8 (2018) 448, https://doi.org/10.3390/catal8100448.

[45] MATLAB R2019b: lsqcurvefit (Version R2019b) [Computer software]. Natick, MA: The MathWorks Inc. Available, (2023). https://fr.mathworks.com/help/optim/ug/lsqcurvefit.html.

[46] M. Iasiello, S. Cunsolo, N. Bianco, W.K.S. Chiu, V. Naso, Developing thermal flow in open-cell foams, Int. J. Therm. Sci. 111 (2017) 129–137, https://doi.org/10.1016/j.ijthermalsci.2016.08.013.

[47] S. Mancin, C. Zilio, A. Diani, L. Rossetto, Air forced convection through metal foams: experimental results and modeling, Int. J. Heat Mass Transf. 62 (2013) 112–123, https://doi.org/10.1016/j.ijheatmasstransfer.2013.02.050.

[48] V.V. Calmidi, R.L. Mahajan, Forced convection in high porosity metal foams, J. Heat Transfer 122 (2000) 557–565, https://doi.org/10.1115/1.1287793.

[49] E. Bianchi, T. Heidig, C.G. Visconti, G. Groppi, H. Freund, E. Tronconi, Heat transfer properties of metal foam supports for structured catalysts: wall heat transfer coefficient, Catal. Today 216 (2013) 121–134, https://doi.org/10.1016/j.cattod.2013.06.019.